



## Article

# Unconventional materials: the mismatch between electronic charge centers and atomic positions

Jiacheng Gao<sup>a,b,1</sup>, Yuting Qian<sup>a,b,1</sup>, Huaxian Jia<sup>a,b,1</sup>, Zhaopeng Guo<sup>a,b</sup>, Zhong Fang<sup>a,b</sup>, Miao Liu<sup>a,b,\*</sup>, Hongming Weng<sup>a,b,\*</sup>, Zhijun Wang<sup>a,b,\*</sup>

<sup>a</sup>Beijing National Laboratory for Condensed Matter Physics, and Institute of Physics, Chinese Academy of Sciences, Beijing 100190, China

<sup>b</sup>University of Chinese Academy of Sciences, Beijing 100049, China

## ARTICLE INFO

## Article history:

Received 2 November 2021

Received in revised form 15 December 2021

Accepted 21 December 2021

Available online 4 January 2022

## Keywords:

Unconventional materials

Band representations

Real-space invariants

Thermoelectric materials

## ABSTRACT

The complete band representations (BRs) have been constructed in the work of topological quantum chemistry. Each BR is expressed by either a localized orbital at a Wyckoff site in real space, or by a set of irreducible representations in momentum space. In this work, we define unconventional materials with a common feature of the mismatch between average electronic centers and atomic positions. They can be effectively diagnosed as whose occupied bands can be expressed as a sum of elementary BRs (eBRs), but not a sum of atomic-orbital-induced BRs (aBRs). The existence of an essential BR at an empty site is described by nonzero real-space invariants (RSIs). The “valence” states can be derived by the aBR decomposition, and unconventional materials are supposed to have an *uncompensated* total “valence” state. The high-throughput screening for unconventional materials has been performed through the first-principles calculations. We have discovered 423 unconventional compounds, including thermoelectric materials, higher-order topological insulators, electrides, hydrogen storage materials, hydrogen evolution reaction electrocatalysts, electrodes, and superconductors. The diversity of these interesting properties and applications would be widely studied in the future.

© 2022 Science China Press. Published by Elsevier B.V. and Science China Press. All rights reserved.

## 1. Introduction

For the past decade, topological insulators (TIs) and semimetals have been intensively studied [1–16]. Many exotic physical properties are proposed in the topological materials, such as spin-momentum-locking Dirac-cone surface states, quantum anomalous Hall effect, Fermi-arc states, negative magnetoresistivity, and chiral anomaly, which have attracted broad interest in condensed matter physics [12–17]. Recently, topological quantum chemistry (TQC) [18,19] and related theories [20,21] provided a general framework to diagnose whether the band structure of a material is topological from irreducible representations (irreps) at several high-symmetry  $k$ -points (HSKPs). If the irreps of a band structure are the same as those of a band representation (BR) in TQC, which is a space group representation formed by exponentially decayed symmetric orbitals in real space, representing a triv-

ial (atomic) insulator, then the band structure is consistent with topologically trivial state; otherwise, it must be topological (Fig. 1). However, among topologically trivial compounds, we have overlooked a large amount of unconventional materials, whose occupied bands can be decomposed as a sum of elementary BRs (eBRs, i.e., generators of BRs), but not a sum of atomic-orbital-induced BRs (aBRs). They possess the unconventional feature of the mismatch between the average electronic centers and the atomic positions (previously known as obstructed atomic limits [8,18,22]). In fact, many interesting properties, such as low work function, strong hydrogen affinity, and electrocatalysis, can be expected in these unconventional materials.

In this work, we have performed the high-throughput screening for unconventional materials in the materials database. We have computed irreps at maximal HSKPs in density-functional theory (DFT) calculations. The aBRs are generated from atomic configurations and positions in a crystal. Based on compatibility relations (CRs) and BRs of the TQC, the BR decomposition of an unconventional material is solved to be a sum of eBRs, but not a sum of aBRs, e.g., “aBRs + an essential BR” (Fig. 2). The essentiality of the BR is described by nonzero RSIs on an empty site. One can derive the

\* Corresponding authors.

E-mail addresses: [mliu@iphy.ac.cn](mailto:mliu@iphy.ac.cn) (M. Liu), [hmweng@iphy.ac.cn](mailto:hmweng@iphy.ac.cn) (H. Weng), [wzj@iphy.ac.cn](mailto:wzj@iphy.ac.cn) (Z. Wang).

<sup>1</sup> These authors contributed equally to this work.

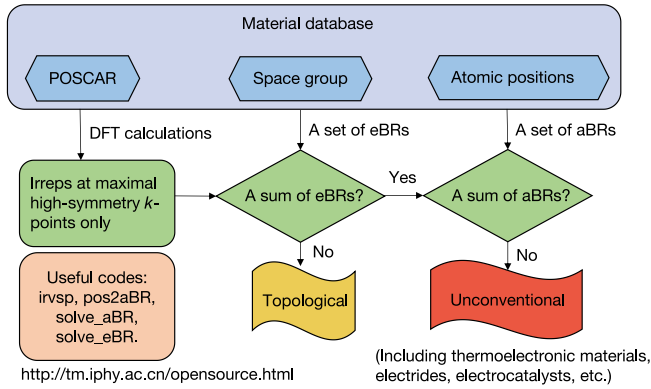


**Fig. 1.** (Color online) The workflow of high-throughput screening for unconventional materials by solving eBR/aBR decomposition in the theory of TQC. Some useful codes are released online (<http://tm.iphy.ac.cn/UnconvMat.html>). Unconventional materials possess the common feature of the mismatch between average electronic centers and atomic positions, where a diversity of interesting properties are expected, such as low work function, strong hydrogen affinity, electrocatalysis, etc.

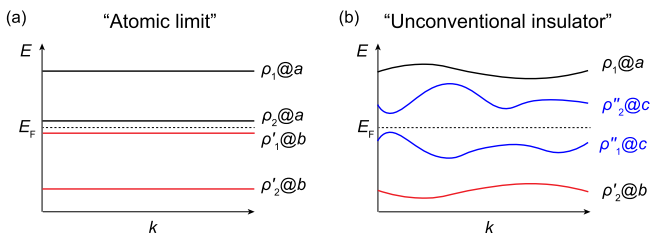


**Fig. 2.** (Color online) Schematic diagram of an unconventional compound  $AB$ . The elements  $A$  and  $B$  sit at the  $a$  and  $b$  Wyckoff sites, respectively. (a) Energy “bands” for the hypothetical structure with large (infinite) lattice constants (i.e., atomic limit). Each set of flat bands is an aBR formed by atomic orbitals, e.g.,  $A-s, A-p, B-s, B-p$ , etc. (b) Energy bands for the synthesized crystal (with experimental lattice constants). The aBR decomposition for occupied bands is solved to be  $\rho_2@b + \rho'_1@c$  (which is empty/hollow in the crystal).

“valence” states from the solved aBRs. The unconventional materials are supposed to be a group of materials with an uncompensated total “valence” state. We find 423 unconventional compounds and tabulate their detailed information in the [Supplementary materials](#). A diversity of interesting properties have been discovered in these compounds, including thermoelectric materials, higher-order TIs, electrides, solid-state hydrogen storage materials, hydrogen evolution reaction (HER) electrocatalysts, electrodes, and superconductors.

## 2. Calculation method

We swept through materials with the Inorganic Crystal Structure Database (ICSD) numbers on the atomly website (<https://atomly.net>). The Vienna *ab-initio* simulation package (VASP) [23,24] with the projector augmented wave method [25,26] based on density functional theory was employed for the first-principles calculations. The generalized gradient approximation of Perdew-Burke-Ernzerhof type [27] was adopted for the exchange-correlation potential. The cutoff energy of plane wave basis set was set to be 125% ENMAX value in the pseudopotential file. A  $\Gamma$ -centered grid with 30  $k$ -points per  $1/\text{\AA}$  was used for self-

consistent calculations. For simplicity, we did not consider any magnetic configurations in the calculations. Electron-phonon coupling calculations were performed in the framework of density functional perturbation theory, as implemented in the QUANTUM ESPRESSO package [28].

The general workflow of our high-throughput screening is given in [Fig. 1](#). First, we obtain the crystal structures of synthesized compounds in the materials database (i.e., atomic elements, Wyckoff positions, and space group number). In TQC theory, a set of eBRs are well defined for a certain space group, while the list of aBRs is defined by atomic elements and positions in a crystal, generated by a homemade program pos2aBR [8] ([https://github.com/zjwang11/UnconvMat/blob/master/src\\_pos2aBR.tar.gz](https://github.com/zjwang11/UnconvMat/blob/master/src_pos2aBR.tar.gz)). Then, the electronic states at maximal HSKPs are obtained in DFT calculations and their irreps are assigned by the program IRVSP [29] ([https://github.com/zjwang11/irvsp/blob/master/src\\_irvsp\\_v2.tar.gz](https://github.com/zjwang11/irvsp/blob/master/src_irvsp_v2.tar.gz)). Since spin-orbit coupling is not included, the obtained irreps are single-valued. Next, we check if these irreps can be decomposed into a sum of eBRs (eBR decomposition, <http://tm.iphy.ac.cn/UnconvMat.html>). If yes, we further check if they are a sum of aBRs (aBR decomposition, <http://tm.iphy.ac.cn/UnconvMat.html>). When they are a sum of eBRs but not a sum of aBRs, we come across an unconventional material. The full list of unconventional materials in our searching is tabulated in the [Supplementary materials](#).

## 3. Results and discussion

### 3.1. Basic concepts in the TQC

The TQC theory tabulates the CRs for 230 space groups, and constructs a complete list of BRs. The CRs suggest that the symmetry eigenvalues of a band structure rely on the irreps only at maximal HSKPs. For a given space group, a certain orbital (irrep  $\rho$ ; labelled by the site-symmetry group) at a Wyckoff site ( $q$ ) can form a bundle of energy bands in momentum space (labelled by a set of irreps of  $\rho@q$  in the space group). The set of irreps is usually regarded as a BR of  $\rho@q$  in the space group. The topologically trivial band structure is a sum of eBRs. On the other hand, by matching the irreps of a band structure with the BRs, one can infer that the band structure belongs to a certain (elementary) BR (i.e.,  $\rho_0@q_0$ ), which tells the average charge center ( $q_0$ ) and the site-symmetry character ( $\rho_0$ ). The BR analysis/decomposition can be widely used in materials computation.

#### 3.1.1. The aBR decomposition

The electronic states of a compound originate from the BRs induced by its atomic orbitals. In the hypothetical structure ([Fig. 2a](#)), the “flat” bands are the original aBRs. After hybridization, the reconstructed occupied bands of unconventional materials can be a sum of eBRs, but not a sum of aBRs. After solving the aBR decomposition ([Fig. 3](#)), the occupied bands of topologically trivial insulators can be generally classified into two cases: (1) solved to be a sum of aBRs, e.g., zinc-blende structure ZnO (conventional); or (2) not a sum of aBRs, such as some aBRs + an essential BR for  $\text{Ca}_2\text{As}$  (unconventional). In the latter case, the essential BR tells the average charge center (i.e., an empty site) and the site-symmetry character of the “loose” electrons.

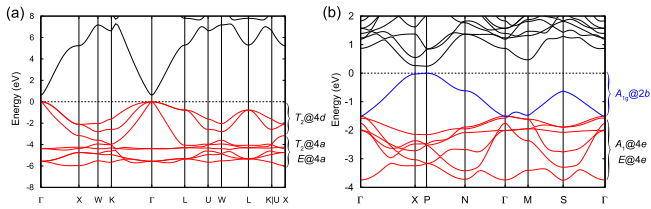


**Fig. 3.** (Color online) Band structures of (a) conventional ZnO and (b) unconventional  $\text{Ca}_2\text{As}$  compounds. The aBR decompositions for occupied bands are presented in the figure.

### 3.1.2. “Valence” states from the aBR decomposition

In both cases, one can derive atomic “valence” states from the solved aBRs of the crystal. Hereafter, valence states in this work are referred to the TQC “valence” states based on the aBR decomposition. The irreps for the occupied bands of ZnO are obtained at four HSKPs in the [Supplementary materials](#). The aBR decomposition is solved to be  $E@4a + T_2@4a + T_2@4d$  (denoted by “Yes” in the last column of [Table 1](#)), corresponding to Zn  $d$  and O  $p_{x,y,z}$  orbitals, respectively. Considering the atomic configurations of Zn and O, one can conclude that their valence states are  $\text{Zn}^{2+}$  and  $\text{O}^{2-}$ . Thus, the insulator ZnO has a compensated total valence state. However, in  $\text{Ca}_2\text{As}$ , the aBR decomposition for its occupied bands is  $A_1@4e + E@4e + A_{1g}@2b$ . Hereafter, the BR colored in blue indicates the essential BR at an empty site. The  $A_1@4e$  and  $E@4e$  aBRs correspond to As  $p_z$  and  $p_{x,y}$  orbitals. The valence states are derived to be  $\text{Ca}^{2+}$  and  $\text{As}^{3-}$ . The uncompensated total valence state (+1) implies that it is unconventional, which is consistent with the electroneutrality nature [\[8,30\]](#).

### 3.1.3. The essential BR and real-space indicators

The essential BR of an empty site can be described by the RSIs, which are local quantum numbers at a Wyckoff site protected by its site-symmetry group (isomorphic to point-group symmetry). The RSIs were introduced to characterize the topological fragile phases and determine the number of gap closings under the specific twisted boundary conditions in 2D [\[31\]](#). Here we generalize the concept of the RSIs to all Wyckoff sites in 230 space groups, especially for maximum Wyckoff sites. The essentiality of the BR for an unconventional insulator is described by the non-zero RSIs on an empty site.

In the atomic limit of an unconventional insulator (hypothetical structure; [Fig. 2a](#)), the RSI is zero on the empty site, while it becomes nonzero in the synthesized crystal ([Fig. 2b](#)). The charge

centers of occupied electronic bands can not move away from the empty site symmetrically without closing the band gap. The essential BR at the empty site implies the disagreement between average electronic centers and atomic positions.

## 3.2. Unconventional insulators

### 3.2.1. Intermetallic semiconductors

Firstly, in the searching results, there are many unconventional semiconductors with only metallic elements, which are known as intermetallic semiconductors in literatures [\[32–34\]](#). Semiconducting substances form one of the most important families of functional materials. However, semiconductors containing only metals are very rare. The chemical mechanisms behind their ground-state properties are not fully understood. Our investigations into unconventional materials can reveal the semiconducting behaviour in the intermetallic compounds and provide an effective way to search for them by computing the irreps at several HSKPs only.

We take  $\text{Be}_5\text{Pt}$  and Na-hP4 as two representatives. Their band structures are shown in [Fig. 4a and b](#), where we can find there are clear band gaps at  $E_F$ . The list of aBRs is given in [Table 2](#). With the computed irreps, the aBRs decomposition of  $\text{Be}_5\text{Pt}$  are solved (i.e.,  $E@4a + T_2@4a + A_1@16e + A_1@4b$ ) and given in the last column (denoted by “yes”), suggesting that one Be(2)-s and five Pt- $d$  orbitals are occupied. Thus, one can derive the valence state for each Wyckoff atom, which is presented in the 5th column of [Table 2](#). The results of Na-hP4 are presented in [Table 2](#) as well. The uncompensated valence state in total reveals that there is an essential BR, i.e.,  $A_1@4b$  for  $\text{Be}_5\text{Pt}$  and  $A'_1@2c$  for Na-hP4. In addition, some thermoelectric materials ( $\text{Al}_2\text{Ru}$ ,  $\text{AlVFe}_2$ , etc.) are also unconventional intermetallic semiconductors.

The hard X-ray photoelectron spectroscopy experiment [\[32\]](#) of  $\text{Be}_5\text{Pt}$  shows a complete filling of Pt- $5d$  levels. The higher binding energy of Be(1)-s than Be(2)-s reflects the difference of valence states between Be(1) and Be(2). These facts are consistent with the aBR analysis. The electrical resistivity measured on bulk samples shows a metal-like temperature dependence, while for the microscale samples, it decreases monotonically with increasing temperature, corresponding to a semiconducting behaviour inferred from the band-structure calculations [\[32\]](#). In [Fig. 4c](#), the in-gap surface states emerge in the slab calculation of  $\text{Be}_5\text{Pt}$ , where the (001) termination cuts through the empty site of the essential BR. We conjecture that its flatness at low temperatures in microscale samples and the semimetallic behaviour in bulk samples

**Table 1**

The aBRs, BR decompositions and valence states are obtained for  $F43m$  zinc-blende ZnO and  $I4/mmm$   $\text{Ca}_2\text{As}$ .

	Atom	WKS( $q$ )	Symm.	States	Conf.	Irreps( $\rho$ )	aBRs( $\rho@q$ )	Occ. <sup>a</sup>
$F43m$ ZnO	Zn	4a	$\bar{4}3m$	$\text{Zn}^{2+}$	$4s^2 3d^{10}$	$s$	$A_1@4a$	
						$d_{z^2, x^2}$	$E@4a$	Yes
	O	4d	$\bar{4}3m$	$\text{O}^{2-}$	$2p^4$	$d_{xy, yz, xz}$	$T_2@4a$	Yes
$I4/mmm$ $\text{Ca}_2\text{As}$	As	4e	$4mm$	$\text{As}^{3-}$	$4p^3$	$p_z$	$A_1@4e$	Yes
						$p_{x,y}$	$E@4e$	Yes
	Ca(1)	4e	$4mm$	$\text{Ca}^{2+}$	$4s^2$	$s$	$A_1@4e$	
	Ca(2)	4c	$mmm$	$\text{Ca}^{2+}$	$4s^2$	$s$	$A_g@4c$	
							$A_{1g}@2b$	Yes

<sup>a</sup> The last column of the table denotes whether the aBR can be decomposed from the occupied energy bands.

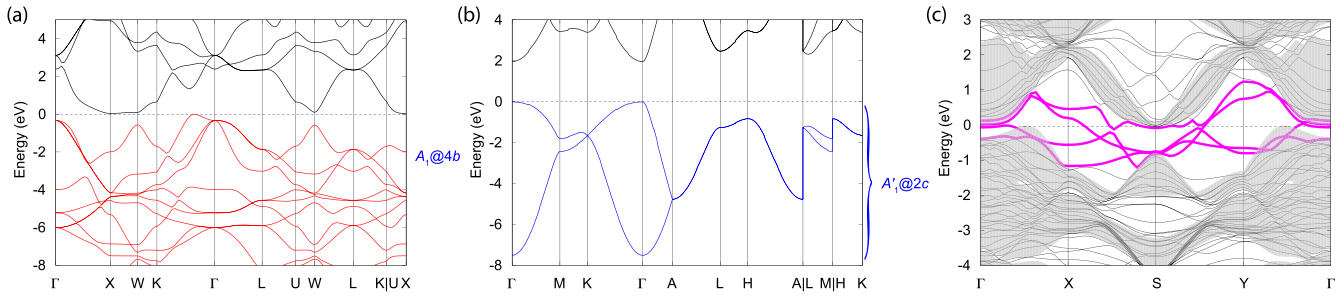


**Fig. 4.** (Color online) Band structures of intermetallic semiconductors (a)  $\text{Be}_5\text{Pt}$  and (b)  $\text{Na-hP4}$ , where the essential BRs are indicated. (c) In-gap surface states in the slab calculation of  $\text{Be}_5\text{Pt}$ . The projected bulk band structure is shown in gray (shaded area).

**Table 2**  
The aBRs, BR decompositions and valence states for the unconventional intermetallic semiconductors.

	Atom	WKS( $q$ )	Symm.	States	Conf.	Irreps( $\rho$ )	aBRs( $\rho@q$ )	Occ.
$F43m$ $\text{Be}_5\text{Pt}$	Pt	$4a$	$43m$	$\text{Pt}^0$	$6s^1 5d^9$	$s$ : $A_1$	$A_1@4a$	
						$d_{z^2, x^2}$ : $E$	$E@4a$	Yes
	Be(1)	$4d$	$\bar{4}3m$	$\text{Be}^{2+}$	$2s^2$	$d_{xy, xz, yz}$ : $T_2$	$T_2@4a$	Yes
	Be(2)	$16e$	$3m$	$\text{Be}^0$	$2s^2$	$s$ : $A_1$	$A_1@4d$	
						$s$ : $A_1$	$A_1@16e$	Yes
							$A_1@4b$	Yes
$P6_3/mmc$ $\text{Na-hP4}$	Na(1)	$2a$	$\bar{3}m$	$\text{Na}^{1+}$	$3s^1$	$s$ : $A_{1g}$	$A_{1g}@2a$	
	Na(2)	$2d$	$\bar{6}2m$	$\text{Na}^{1+}$	$3s^1$	$s$ : $A'_1$	$A'_1@2d$	
							$A'_1@2c$	Yes

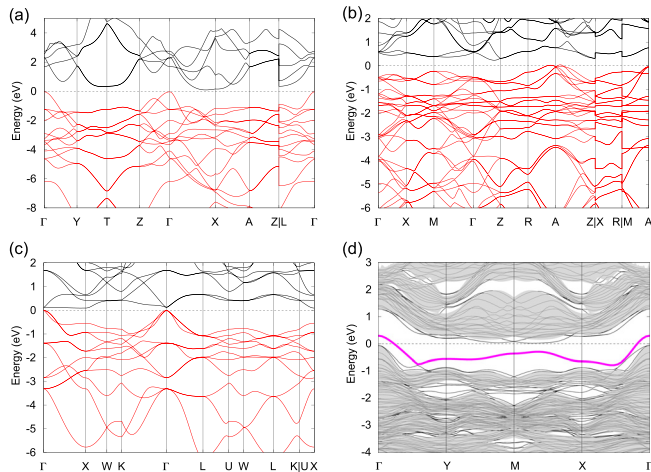


**Fig. 5.** (Color online) Band structures of thermoelectric materials. (a)  $\text{Al}_2\text{Ru}$  has the essential BR of  $A_g@16d$ . (b)  $\text{In}_3\text{Ru}$  has the essential BR of  $A_g@2b$ . (c)  $\text{TiFe}_2\text{Sn}$  has the essential BR of  $A_g@24d$ . (d) Surface states in the slab calculation of  $\text{Al}_2\text{Ru}$ . The projected bulk band structure is shown in gray (shaded area).

are contributed to the existence of surface states on the grain boundaries.

### 3.2.2. Thermoelectric materials

Secondly, many unconventional semiconductors are formed by transition metals and Group 13–15 ( $p$ -block) elements, such as  $\text{Al}_2$ -

$\text{Ru}/\text{Ga}_2\text{Ru}$ ,  $\text{In}_3\text{Ru}/\text{Ga}_3\text{Ir}$ , and  $\text{TiFe}_2\text{Sn}/\text{AlVFe}_2/\text{VGaFe}_2$  (i.e., Heusler compounds  $\text{XY}_2\text{Z}$  with 24 valence electrons), which were previously known as thermoelectric materials [34–40]. The band structures of  $\text{Al}_2\text{Ru}$ ,  $\text{In}_3\text{Ru}$  and  $\text{TiFe}_2\text{Sn}$  are shown in Fig. 5. The aBR decompositions for occupied bands of these materials are solved. The results in Table 3 indicate that the essential BR is  $A_g@16d$  for  $\text{Al}_2\text{Ru}/\text{Ga}_2\text{Ru}$ ,  $A_g@2b$  for  $\text{In}_3\text{Ru}$ , and  $A_g@24d$  for  $\text{TiFe}_2\text{Sn}/\text{AlVFe}_2/\text{VGaFe}_2$ . Thermoelectric properties, superparamagnetism and negative giant magnetoresistance have been widely studied in these Heusler compounds  $\text{XY}_2\text{Z}$  with 24 valence electrons [39,41–43].

As we know, the thermoelectric efficiency of materials at temperature  $T$  is characterized through the figure of merit given by the relation  $zT = S^2\sigma T/\kappa$ , where  $S$  is the thermoelectric or Seebeck coefficient,  $\sigma$  is the electronic conductivity and  $\kappa$  is the thermal conductivity. The essential BRs of the unconventional materials suggest that surface states can emerge and conduct electricity when the surface cuts through the empty sites. The in-gap surface states are obtained in the (001)-slab calculation of  $\text{Al}_2\text{Ru}$  in Fig. 5d. The insulating bulk states suggest that thermal conductivity due to bulk carries is weak. But the electronic conductivity due to the grain boundaries is substantial. These properties are beneficial to the thermoelectric efficiency of these unconventional semiconductors.

### 3.2.3. Higher-order topological insulators

Thirdly, the nonmetal materials used to be known as covalent compounds. As the common covalent state has the average charge center located on  $X-X$  bonds, the covalent compounds would fit

**Table 3**  
The aBRs, BR decompositions and valence states for  $Fddd$   $Al_2Ru$ ,  $P4_2/mnm$   $In_3Ru$ ,  $Fm\bar{3}m$   $TiFe_2Sn/AIVFe_2$ .

	Atom	WKS( $q$ )	Symm.	States	Conf.	Irreps( $\rho$ )		aBRs( $\rho@q$ )	Occ.	
$Fddd$ $Al_2Ru$	Al	16f	2	$Al^{1+}$	$3s^23p^1$	$s$	:A	$A@16f$	Yes	
						$p_z$	:A	$A@16f$		
	Ru	8b	222	$Ru^{2+}$	$5s^14d^7$	$p_x/p_y$	:B	$B@16f$	Yes	
						$s$	:A	$A@8b$		
						$d_{z^2}/d_{xz}$	:A	$A@8b$		
						$d_{xy}$	:B <sub>1</sub>	$B_1@8b$		
						$d_{yz}$	:B <sub>3</sub>	$B_3@8b$		
						$d_{xz}$	:B <sub>2</sub>	$B_2@8b$		
								$A_g@16d$	Yes	
	$P4_2/mnm$ $In_3Ru$	Ru	4f	$mm2$	$Ru^0$	$5s^14d^7$	$s$	:A <sub>1</sub>	$A_1@4f$	Yes
$d_{xz}$							:A <sub>1</sub>	$A_1@4f$		
$d_{z^2}$							:A <sub>1</sub>	$A_1@4f$		
$d_{xy}$							:A <sub>2</sub>	$A_2@4f$		
$d_{yz}$							:B <sub>2</sub>	$B_2@4f$		
In		4c	$2/m$	$In^{1-}$	$5s^25p^1$	$d_{xz}$	:B <sub>1</sub>	$B_1@4f$	Yes	
						$s$	:A <sub>g</sub>	$A_g@4c$		
						$p_z$	:A <sub>u</sub>	$A_u@4c$		
						$p_x$	:B <sub>u</sub>	$B_u@4c$		
						$p_y$	:B <sub>u</sub>	$B_u@4c$		
In		8j	$m$	$In^{1+}$	$5s^25p^1$	$s$	:A'	$A'@8j$	Yes	
						$p_x$	:A'	$A'@8j$		
						$p_y$	:A'	$A'@8j$		
						$p_z$	:A''	$A''@8j$		
$Fm\bar{3}m$ $TiFe_2Sn$ ( $AIVFe_2$ )	Fe	8c	$\bar{4}3m$	$Fe^{2+}$	$3d^74s^1$	$s$	:A <sub>1</sub>	$A_1@8c$	Yes	
						$d_{z^2}, x^2$	:E	$E@8c$		
	Sn (Al)	4b	$m\bar{3}m$	$Sn^{4+}$ ( $Al^{3+}$ )	$5s^25p^2$ ( $3s^23p^1$ )	$d_{xy}, xz, yz$	:T <sub>2</sub>	$T_2@8c$	Yes	
						$s$	:A <sub>1g</sub>	$A_{1g}@4b$		
	Ti (V)	4a	$m\bar{3}m$	$Ti^{4+}$ ( $V^{5+}$ )	$4s^13d^3$ ( $4s^13d^4$ )	$p_{x,y,z}$	:T <sub>1u</sub>	$T_{1u}@4b$	Yes	
						$s$	:A <sub>1g</sub>	$A_{1g}@4a$		
							$d_{z^2}, x^2$	:E <sub>g</sub>	$E_g@4a$	Yes
							$d_{xy}, xz, yz$	:T <sub>2g</sub>	$T_{2g}@4a$	
								$A_g@24d$	Yes	

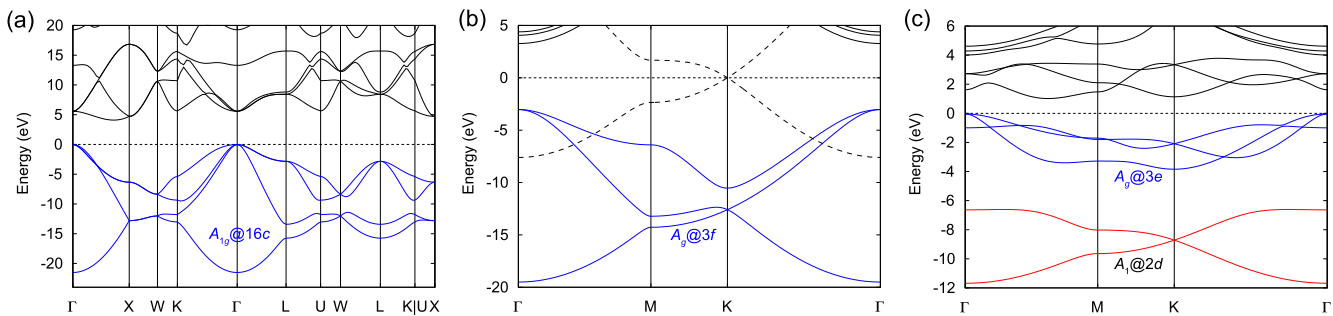


**Fig. 6.** (Color online) Band structures of (a) diamond, (b) graphene and (c)  $\beta$ -antimonene. The essential BRs are shown by blue bands. In graphene, the  $m_z$ -even (-odd) bands are plotted in solid (dashed) lines.

the definition of unconventional materials as well. Since they are well-known and studied, we exclude these compounds without any metal elements in our high-throughput screening for simplicity.

Here, some semiconducting covalent elements can be regarded as higher-order TIs in literature [44–46]. Strictly speaking, The 3rd-

order TIs in 3D and 2nd-order TIs in 2D are topologically trivial (without particle-hole symmetry). However, they are proved to present a filling anomaly: a mismatch between the number of electrons in a symmetric geometry and the number of electrons required for charge neutrality [47]. For example, the 3D crystals of diamond (or silicon) have  $sp^3$  hybridization and the occupied

bands belong to the BR of 16c sites, corresponding to four C – C bond centers (Fig. 6a). In this sense, they can be regarded as a 3rd-order TI in 3D, while the two-dimensional graphene can be regarded as a 2nd-order TI in the  $m_z$ -even subspace (i.e.,  $s$ ,  $p_x$ ,  $p_y$  orbitals). The  $sp^2$  hybridization in graphene can be understood by the BR of 3f sites, corresponding to three C – C bond centers in a unit cell. Note that  $p_z$  orbital belongs to the  $m_z$ -odd subspace, shown as dashed bands in Fig. 6b. In a broad sense, the  $7 \times 7$  reconstruction on Si-(111) surface could be related to the unconventional nature of silicon due to the presence of substantial charge on the terminations.

Recently, the graphene-like buckled structure ( $\beta$ -phase) of Sb was found to have the best stability [48]. The Sb monolayer ( $\beta$ -antimonene) has been successfully exfoliated using micromechanical technology [49], and has been synthesized on various substrates via van der Waals epitaxial growth [50]. The band structure of  $\beta$ -antimonene is obtained in Fig. 6c. The aBR decomposition is solved to be  $A_1@2d + A_g@3e$  (Table 4). The Sb atoms are located at 2d site of space group  $P\bar{3}m1$  (No. 164), while the 3e sites of the essential BR are the centers of Sb–Sb bonds. In terms of charge fractionalization and polarization, it corresponds to the  $h_{3c}^{(6)}$  primitive generator class in Benalcazar et al.'s notation in Ref. [47,51,52]. In a strict way, the primitive generator would be  $h_{3c}^{(3)}$  after generalizing their notations to  $\bar{3}$  layer group. It implies that there is no net dipole in the plane and the corner charge fractionalization will be  $e/2$  in each  $\pi/6$  sector in the spinless case and  $e$  in the spinful case. We note that even though it is the inversion that protects the edge states, hosting corner states at all corners require the presence of the  $S_6$  ( $\equiv IC_3$ ) symmetry operation and a hexagon-shaped island.

### 3.3. Unconventional metals

Then, we can generalize the concept of unconventional insulators into unconventional “neat” metals. A “neat” metallic compound is supposed to have an overall band gap shadowed about/above  $E_F$  in Fig. 7. We classify them into three classes. In class I, e.g., VGaFe<sub>2</sub> in Fig. 7a, there is a direct energy gap in the band structure, while there is no global gap in the entire Brillouin zone. In class II, e.g., Ca<sub>2</sub>N in Fig. 7b, it is metallic due to the odd total number of electrons. However there would be a gap with one more electron. In class III, e.g., Y<sub>2</sub>C in Fig. 7c, there is an overall band gap except some  $k$ -point; namely, there can be a band inversion.

Unconventional metals are well defined as long as a set of “occupied” bands are defined in the metallic compounds. The occupied states are defined by simply counting energy bands at HSKPs in class I and class II. For complicated metals of class III, one has to work a little bit to get the set of “occupied” bands at HSKPs by solving CRs. We need to eliminate the band inversion via switching irreps by hand. The results of unconventional metals

**Table 4**  
The aBRs, BR decomposition and valence states for  $P\bar{3}m1$   $\beta$ -antimonene.

Atom	WKS ( $q$ )	Symm.	States	Conf.	Irreps( $\rho$ )	aBRs ( $\rho@q$ )	Occ.
Sb	2d	3m	Sb <sup>3+</sup>	5s <sup>2</sup> 5p <sup>3</sup>	$s$	$A_1@2d$	Yes
					$p_z$	$A_1@2d$	
					$p_x, p_y$	$E@2d$	
						$A_g@3e$	

contain many functional materials, such as electrides, solid-state hydrogen storage materials, and HER electrocatalysts.

#### 3.3.1. Electrides

An electride is usually defined as an ionic crystal with excess electrons confined in particular vacancies, which is an excellent example of unconventional metals [8,53]. To achieve an electride, it is empirically known that three criteria should be satisfied: excess electrons, lattice vacancies, and suitable electronegativity of the elements. By the definition, the electrides are consistent with unconventional materials. They have an essential BR, which is not induced by any atomic orbitals in the crystal, but formed by the electrons at the vacancies. Therefore, there are many electride candidates picked out by our high-throughput screening for unconventional materials, like Ca<sub>2</sub>N and Ca<sub>2</sub>As. Additionally, as we did in Refs. [8,53], the electrides (i.e., Y<sub>2</sub>C, LaCl, Li<sub>12</sub>Mg<sub>3</sub>Si<sub>4</sub> and C12A7) with relatively complicated band structures are also diagnosed by the aBR decomposition. The calculated band structures and partial electron density (PED) are shown in Fig. 8.

The previous search for electrides is done mainly by analyzing charge density around  $E_F$ , where electron localization function (ELF) analysis has proved to be effective. However, the symmetry analysis is lacking. By analyzing the symmetry eigenvalues (or irreps) alone at several HSKPs in first-principles calculations, the BR analysis of TQC theory leads to the clear understanding of three characteristics of electrides as discussed in Ref. [8]. First, the floating bands are induced from the BRs of vacancies, indicating that their average charge densities are located at the vacancies in real space. Second, due to the loose confinement, the floating bands are usually close to the  $E_F$ , which is very likely to induce the band inversion and nontrivial band topology. Third, the excess anionic electrons in vacancies present a strong hydrogen affinity. The absorption of hydrogen usually moves those floating bands far below  $E_F$  and lowers the total energy (stabilizing the lattice). A significant amount of hydrogen is found experimentally in the crystals of Lanthanum monochloride [54] and Ca<sub>5</sub>P<sub>3</sub> crystals [55]. Note that an unconventional material is necessary but not sufficient for an electride. For safety, one may need to compute the charge distribution to confirm electride nature in the selected unconventional materials.

#### 3.3.2. Solid-state hydrogen storage materials

We found some unconventional metal alloys, LiAl/LiB [56,57], which are well-known solid-state hydrogen storage materials. When the hydrogen molecule comes in contact with the surface of solid-state hydrogen storage materials, it dissociates into two hydrogen atoms which diffuse in the solid and form a chemical bond with the solid material (i.e., metal hydrides). The crystals of LiAl have the structure of  $Fd\bar{3}m$  (No. 227). The eight valence electrons (two formulas per unit cell) form the bands of the BR  $A_{1g}@16d$  (which is empty). Hydrogen forms metal hydrides with some metals and alloys, leading to solid state storage under moderate temperature and pressure that gives them important safety advantages over the gaseous and liquid storage methods. Hence, metal hydride storage is a safe, volume-efficient storage method for on-board vehicle applications.

Then, we also check the unconventional metal TiFe of class III by hand [58,59]. In its band structure of Fig. 9c, there is an overall band gap except two band inverted HSKPs, i.e., X and M. After removing the band inversions (exchanging the irreps denoted by triangles and circles), the “occupied” bands are solved to be  $A_{1g}@1b + T_{2g}@1a + A_{1g}@3d$ . It can be seen clearly that the bands of the essential BR appear around  $E_F$ . By absorbing the hydrogen

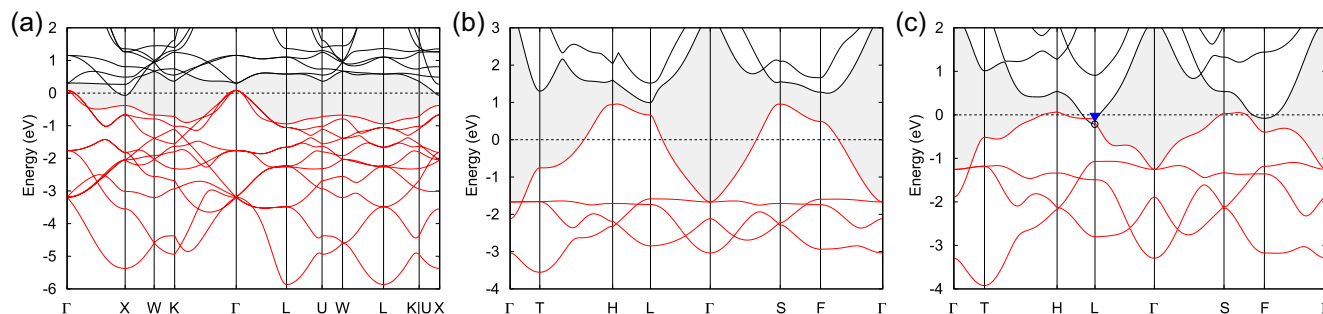


**Fig. 7.** (Color online) Three classes of unconventional “neat” metals, where there is almost a direct band gap (indicated by shaded area) about/above  $E_F$ . (a)  $\text{VGaFe}_2$  of class I: there is a direct energy gap in the band structure, while there is no global gap for the entire Brillouin zone. (b)  $\text{Ca}_2\text{N}$  of class II: it is metallic due to the odd total number of electrons. However there would be a gap with one more electron. (c)  $\text{Y}_2\text{C}$  of class III: there is an overall band gap except some  $k$ -point; namely, there can be a band inversion, denoted by a circle and a triangle.

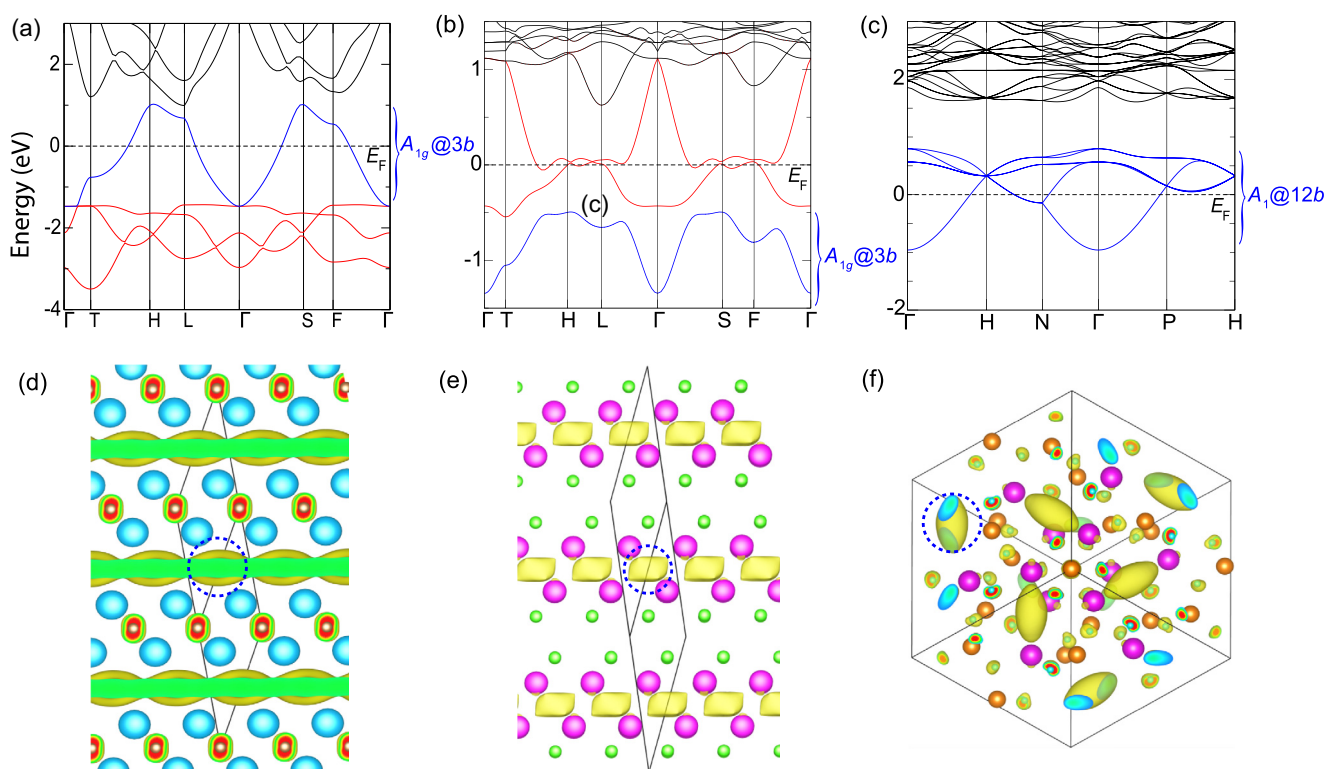


**Fig. 8.** (Color online) (a–c) Band structures of the electrides:  $\text{Ca}_2\text{N}$ ,  $\text{LaCl}$ , and  $\text{C12A7}$ , respectively. (d–f) The calculated PED of the blue-colored bands for  $\text{Ca}_2\text{N}$ ,  $\text{LaCl}$ , and  $\text{C12A7}$ , respectively, with the dashed blue circles marked the essential site (adapted from Ref. [8]).

atoms on  $3d$  site, the energy bands of the essential BR decrease dramatically as shown in Fig. 9d.

### 3.3.3. Electrocatalysts and electrodes

The orthogonal  $\text{NiP}$  and cubic  $\text{NiP}_2$  compounds are found to be unconventional metals. The essential BR is solved to be  $A_g@4a$  for  $\text{NiP}$  and  $A_{1g}@4b$  for  $\text{NiP}_2$ . The band structure of cubic  $\text{NiP}_2$  is presented in Fig. 10. To show that the electronic centers are not located at the atoms, the ELF is plotted for  $\text{NiP}_2$  in Fig. 10b. On the other hand, the HER, which generates molecular hydrogen through the electrochemical reduction of water, underpins many

clean-energy technologies [60,61]. The pyrite structure-type transition metal dichalcogenides ( $\text{MX}_2$ , where  $M = \text{Fe}, \text{Co},$  or  $\text{Ni}$  and  $X = \text{S}$  or  $\text{Se}$ ) have emerged as an interesting family of low-cost materials with high catalytic activity toward the HER [62]. We believe that these maximum electron distributions offset from the atomic positions benefit to catalyze electrochemical reaction, such as HERs and negative electrodes for Li-ion batteries [63,64].

Additionally, the aBR decomposition for the skutterudite-type  $\text{CoP}_3$  compound suggests that it is unconventional with band inversion. From the plotted band structure in Fig. 10c, one can find that the band inversion happens between low-energy states at  $\Gamma$ ,

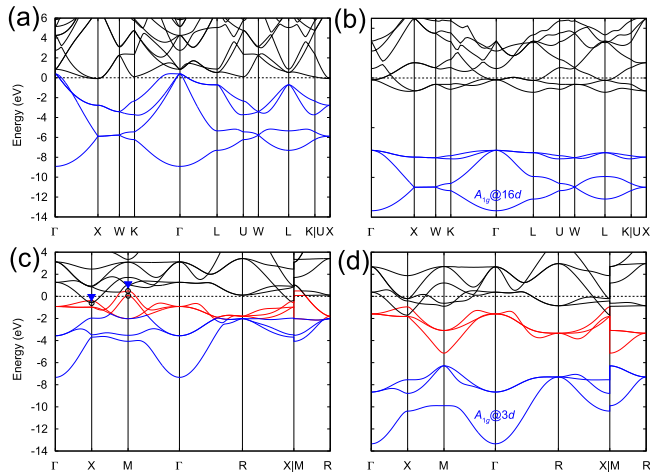


**Fig. 9.** (Color online) Band structures of (a) LiAl and (c) TiFe. Panels (b) and (d) present the band structures after absorbing hydrogen atoms at the empty sites.

denoted by a circle and a triangle, respectively. The electrochemical reaction of lithium with the  $\text{CoP}_3$  compound has been studied in Refs. [65].  $\text{Co}_{1-x}\text{Ni}_x\text{P}_3$  exhibits much better electronic properties for obtaining high energy density supercapacitors [66] and  $\text{NiP}_3$  is

proved to be a promising negative electrode for Li- and Na-ion batteries [67].

### 3.3.4. Superconductors

The compound  $\text{Zr}_5\text{Sb}_3$  is experimentally found to be the first superconductor in the large family of compounds with  $\text{Mn}_5\text{Si}_3$ -type structure (No. 193) [68], which is believed to be superconducting due to the electron-phonon coupling. The superconducting transition temperature ( $T_c$ ) is estimated using Allen-Dynes modified McMillian equation [69,70],

$$T_c = \frac{\omega_{\text{log}}}{1.2k_B} \exp\left[\frac{-1.04(1 + \lambda)}{\lambda(1 - 0.62\mu^*) - \mu^*}\right], \quad (1)$$

where  $k_B$  is the Boltzmann constant,  $\mu^*$  is the effective screened Coulomb repulsion constant, typically  $\sim 0.1$ ,  $\lambda = \sum_{\mathbf{q}\nu} \lambda_{\mathbf{q}\nu}$  is logarithmic average phonon frequency. With  $\mu^* = 0.10$  and  $\lambda = 0.53$ ,  $T_c$  of  $\text{Zr}_5\text{Sb}_3$  is estimated to be 2.2 K, which is consistent to the experimental value ( $\sim 2.3$  K) [68]. The phonon spectrum of  $\text{Zr}_5\text{Sb}_3$  is shown in Fig. 11a. The contributions of  $\lambda$  mainly come from the phonon modes of  $50 \text{ cm}^{-1} < \omega < 150 \text{ cm}^{-1}$ . Among these phonon modes, we find that the low-frequency  $B_{1u}$  phonon mode at  $\Gamma$  has higher  $\lambda_{\mathbf{q}\nu}$  than others. As shown in Fig. 11b, the  $B_{1u}$  phonon mode is an in-plane vibration mode of  $\text{Zr}(2)$  atoms, which form triangles in  $z = 0.25c$  and  $z = 0.75c$  planes.

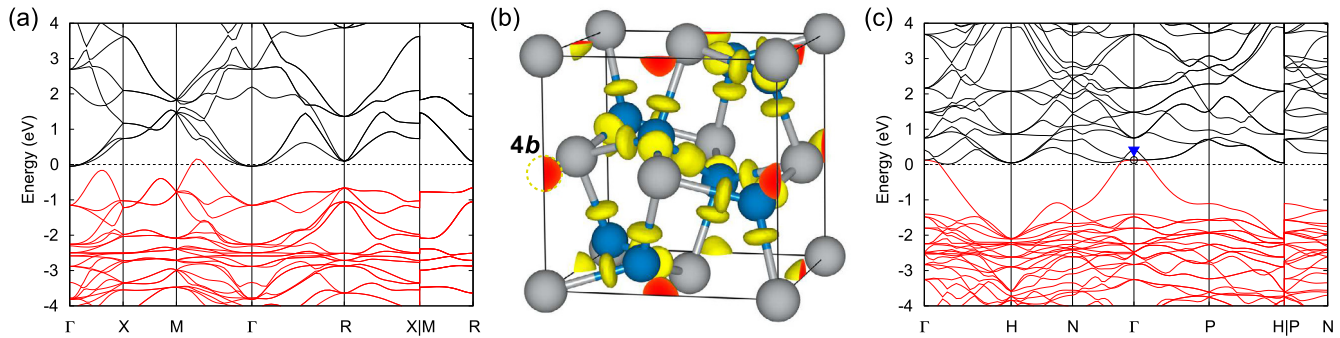


**Fig. 10.** (Color online) Band structures of (a)  $\text{NiP}_2$  and (c)  $\text{CoP}_3$ . (b) The ELF plot of  $\text{NiP}_2$ .

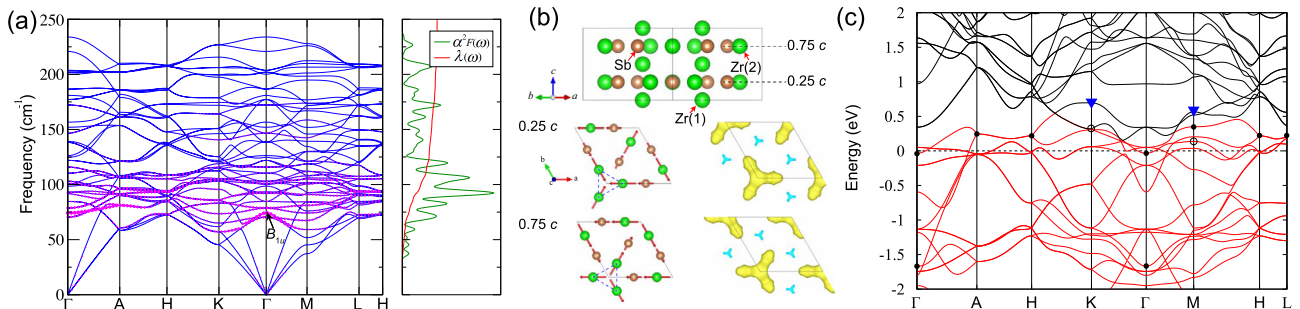


**Fig. 11.** (Color online) (a) Phonon spectrum, Eliashberg spectral functions  $\alpha^2F(\omega)$ , and the frequency-dependent coupling  $\lambda(\omega)$ . The electron-phonon couplings  $\lambda_{\mathbf{q}\nu}$  are represented by magenta circles. (b) Side view of the crystal structure of  $\text{Zr}_5\text{Sb}_3$ . The planes of  $z = 0.25c$  and  $z = 0.75c$  are marked by dash lines. The phonon vibration mode of  $B_{1u}$  is indicated by the arrows, i.e., compression of the triangle in  $z = 0.25c$  plane and expansion of the triangle in  $z = 0.75c$  plane. The calculated PED of bands of the energy range 0.0 to 0.3 eV is shown and coincides with the  $B_{1u}$  phonon mode. (c) The band structure of  $\text{Zr}_5\text{Sb}_3$ . The BR decomposition is solved for the lower 38 energy bands in red. The essential BR is  $A'_1@2a$ .

**Table 5**  
Atomic positions, valence states and aBRs of 38 energy bands in  $P6_3/mcm$   $Zr_5Sb_3$ .

Atom	WKS (q)	Symm.	States	Conf.	Irreps( $\rho$ )	aBRs ( $\rho@q$ )	Occ.					
Zr(1)	4d	32	$Zr^{2-}$	$5s^14d^3$	s	$A_1@4d$	Yes					
					$d_{z^2}$	$A_1$	$A_1@4d$	Yes				
					$d_{xz}, d_{yz}$	$E$	$E@4d$					
					$d_{x^2-y^2}, d_{xy}$	$E$	$E@4d$					
Zr(2)	6g	mm2	$Zr^{4+}$	$5s^14d^3$	s	$A_1$	$A_1@4d$					
					$d_{z^2}$	$A_1$	$A_1@6g$					
					$d_{x^2}$	$A_1$	$A_1@6g$					
					$d_{xy}$	$A_2$	$A_2@6g$					
					$d_{yz}$	$B_2$	$B_2@6g$					
					$d_{xz}$	$B_1$	$B_1@6g$					
Sb	6g	mm2	$Sb^{3-}$	$5s^25p^3$	s	$A_1$	$A_1@6g$	Yes				
					$p_z$	$A_1$	$A_1@6g$	Yes				
					$p_y$	$B_2$	$B_2@6g$	Yes				
					$p_x$	$B_1$	$B_1@6g$	Yes				
											$A'_1@2a$	Yes

In our calculations, the aBR decomposition of  $Zr_5Sb_3$  superconductor suggests that it is a complicated unconventional metallic material. Its band structure is presented in Fig. 11c. One can find that there is an overall band gap between the red-colored bands (corresponding to 76 electrons) and higher energy bands, while two band inversions happen between the bands denoted by circles and triangles at K and M points, respectively. The aBR decomposition is solved to be  $A_1@4d + E@4d + 2A_1@6g + B_1@6g + B_2@6g + A'_1@2a$  (Table 5). The center of the essential BR is 2a site, being the center of the Zr(2) triangle. The energy bands of the essential BR are denoted by black dots, which are located energetically near  $E_F$ . The PED of the bands near  $E_F$  is shown in Fig. 11b, which is consistent with the essential BR. Surprisingly, the electronic distribution of the low-energy states (i.e., the essential BR) coincides with the  $B_{1u}$  phonon mode. It gives rise to strong interaction (higher  $\lambda_{qv}$ ), which contributes mainly to the superconductivity in  $Zr_5Sb_3$ .

Additionally, the authors of Ref. [71] introduced a BR sitting on an empty 1b site (an essential BR) in the minimum tight-binding model in the parent compound  $NdNiO_2$  of Ni-based superconductors, prepared by removing an apical O atom in  $NdNiO_3$ . The 1b site was sat by the apical O atom in the precursor. On the other hand, using DFT calculations, the stoichiometric  $NdNiO_2$  is found to be significantly unstable. Instead, they argue that the H impurity can be expected to be present in  $NdNiO_2$  in Ref. [72]. A detailed aBR decomposition for energy bands of  $NdNiO_2$  is given in the Supplementary materials. It clearly shows that the essential BR of  $A_{1g}@1b$  is around  $E_F$  and could be shifted downwards significantly by absorbing H atom at 1b site. Like the elctrides [54,55], some H impurities should benefit to stabilize the crystal structure, and it would be hard to remove them completely during the preparation.

#### 4. Discussion and conclusion

Due to the limitation of length of this paper, we only discuss on some examples in the main text. More unconventional materials are tabulated in the Supplementary materials. The detailed information, such as ICSD number, chemical formula, number of atoms, number of electrons, direct band gap, indirect gap, space group number, atomic Wyckoff sites, and the essential BR, is presented in Table S3 (online). We believe that there are more interesting functional materials among them.

In conclusion, we demonstrate that the analysis of irreps and BRs in TQC theory provides an effective way to identify the origin of the energy bands from their symmetry eigenvalues (or irreps) alone. The aBR decomposition is efficient to diagnose the mismatch between the average electronic charge centers and the atomic positions in unconventional materials. The essential BR of an empty symmetry site can be described by the nonzero RSIs. It is worth noting that not all unconventional materials can be found by this symmetry-based method (aBR decomposition), especially for those with electronic charge centered on the non-maximal Wyckoff positions. Like topological insulators with zero symmetry-based indicators, there are still some unconventional materials with zero RSIs (a sum of aBRs), which need to be explored in future. The presence of the electronic distribution away from nuclei gives rise to a diversity of interesting properties and applications, such as thermoelectronic materials, higher-order TIs, electrides, hydrogen storage materials, HER electrocatalysts, etc. These interesting properties in unconventional materials would draw broad interest in the future.

Note: During the refereeing stages of this work, we found some works with similar topic appear [73–75].

#### Conflict of interest

The authors declare that they have no conflict of interest.

#### Acknowledgments

This work was supported by the National Natural Science Foundation of China (11974395 and 12188101), the Strategic Priority Research Program of the Chinese Academy of Sciences (XDB33000000), and the Center for Materials Genome. H.W. acknowledges support from the Ministry of Science and Technology of China under Grant Nos. 2016YFA0300600 and 2018YFA0305700, the Chinese Academy of Sciences under Grant No. XDB28000000, the Science Challenge Project (TZ2016004), the K. C. Wong Education Foundation (GJTD-2018-01), Beijing Municipal Science & Technology Commission (Z181100004218001) and Beijing Natural Science Foundation (Z180008).

#### Author contributions

Zhijun Wang, Hongming Weng and Miao Liu proposed and supervised the project. Jiacheng Gao, Yuting Qian and Huaxian Jia carried out the high-throughput calculations. All authors contributed to writing of the manuscript.

#### Appendix A. Supplementary materials

Supplementary materials to this article can be found online at <https://doi.org/10.1016/j.scib.2021.12.025>.

#### References

- [1] Bernevig BA, Hughes TL, Zhang SC. Quantum spin Hall effect and topological phase transition in HgTe quantum wells. *Science* 2006;314:1757–61.
- [2] Hasan MZ, Kane CL. Colloquium: topological insulators. *Rev Mod Phys* 2010;82:3045.
- [3] Qi XL, Zhang SC. Topological insulators and superconductors. *Rev Mod Phys* 2011;83:1057.
- [4] Fu L. Topological crystalline insulators. *Phys Rev Lett* 2011;106:106802.
- [5] Yan B, Felser C. Topological materials: Weyl semimetals. *Annu Rev Condens Matter Phys* 2017;8:337–54.
- [6] Wang Z, Alexandradinata A, Cava RJ, et al. Hourglass fermions. *Nature* 2016;532:189–94.

- [7] Ma J, Yi C, Lv B, et al. Experimental evidence of hourglass fermion in the candidate nonsymmorphic topological insulator KHgSb. *Sci Adv* 2017;3:e1602415.
- [8] Nie S, Qian Y, Gao J, et al. Application of topological quantum chemistry in electrides. *Phys Rev B* 2021;103:205133.
- [9] Song Z, Wang Z, Shi W, et al. All magic angles in twisted bilayer graphene are topological. *Phys Rev Lett* 2019;123:036401.
- [10] Zhang H, Liu CX, Qi XL, et al. Topological insulators in Bi<sub>2</sub>Se<sub>3</sub>, Bi<sub>2</sub>Te<sub>3</sub> and Sb<sub>2</sub>Te<sub>3</sub> with a single Dirac cone on the surface. *Nat Phys* 2009;5:438–42.
- [11] Wang Z, Sun Y, Chen XQ, et al. Dirac semimetal and topological phase transitions in A<sub>3</sub>Bi (A = Na, K, Rb). *Phys Rev B* 2012;85:195320.
- [12] Wang Z, Weng H, Wu Q, et al. Three-dimensional Dirac semimetal and quantum transport in Cd<sub>3</sub>As<sub>2</sub>. *Phys Rev B* 2013;88:125427.
- [13] Weng H, Fang C, Fang Z, et al. Weyl semimetal phase in noncentrosymmetric transition-metal monophosphides. *Phys Rev X* 2015;5:011029.
- [14] Hsieh TH, Lin H, Liu J, et al. Topological crystalline insulators in the SnTe material class. *Nat Commun* 2012;3:1–7.
- [15] Liu QB, Qian Y, Fu HH, et al. Symmetry-enforced Weyl phonons. *NPJ Comput Mater* 2020;6:1–6.
- [16] Gao J, Qian Y, Nie S, et al. High-throughput screening for Weyl semimetals with S<sub>4</sub> symmetry. *Sci Bull* 2021;66:667–75.
- [17] Chang CZ, Zhang J, Feng X, et al. Experimental observation of the quantum anomalous Hall effect in a magnetic topological insulator. *Science* 2013;340:167–70.
- [18] Bradlyn B, Elcoro L, Cano J, et al. Topological quantum chemistry. *Nature* 2017;547:298.
- [19] Vergniory M, Elcoro L, Felser C, et al. A complete catalogue of high-quality topological materials. *Nature* 2019;566:480.
- [20] Po HC, Vishwanath A, Watanabe H. Symmetry-based indicators of band topology in the 230 space groups. *Nat Commun* 2017;8:50.
- [21] Song Z, Zhang T, Fang Z, et al. Quantitative mappings between symmetry and topology in solids. *Nat Commun* 2018;9:3530.
- [22] Cano J, Bradlyn B, Wang Z, et al. Building blocks of topological quantum chemistry: elementary band representations. *Phys Rev B* 2018;97:035139.
- [23] Kresse G, Furthmüller J. Efficiency of *ab-initio* total energy calculations for metals and semiconductors using a plane-wave basis set. *Comput Mater Sci* 1996;6:15–50.
- [24] Kresse G, Furthmüller J. Efficient iterative schemes for *ab initio* total-energy calculations using a plane-wave basis set. *Phys Rev B* 1996;54:11169–86.
- [25] Blöchl PE. Projector augmented-wave method. *Phys Rev B* 1994;50:17953–79.
- [26] Kresse G, Joubert D. From ultrasoft pseudopotentials to the projector augmented-wave method. *Phys Rev B* 1999;59:1758–75.
- [27] Perdew JP, Burke K, Ernzerhof M. Generalized gradient approximation made simple. *Phys Rev Lett* 1996;77:3865–8.
- [28] Giannozzi P, Baroni S, Bonini N, et al. QUANTUM ESPRESSO: a modular and open-source software project for quantum simulations of materials. *J Condens Matter Phys* 2009;21:395502.
- [29] Gao J, Wu Q, Persson C, et al. Irvsp: to obtain irreducible representations of electronic states in the VASP. *Comput Phys Commun* 2021;261:107760.
- [30] Hirayama M, Matsuishi S, Hosono H, et al. Electrides as a new platform of topological materials. *Phys Rev X* 2018;8:031067.
- [31] Song ZD, Elcoro L, Bernevig BA. Twisted bulk-boundary correspondence of fragile topology. *Science* 2020;367:794–7.
- [32] Amon A, Svanidze E, Ormeci A, et al. Interplay of atomic interactions in the intermetallic semiconductor Be<sub>3</sub>Pt. *Angew Chem Int Ed* 2019;58:15928–33.
- [33] Ma Y, Eremets M, Oganov AR, et al. Transparent dense sodium. *Nature* 2009;458:182–5.
- [34] Volkov P, Poon S. Semiconducting behavior of the intermetallic compound Al<sub>2</sub>Ru. *EPL* 1994;28:271.
- [35] Takagiwa Y, Matsubayashi Y, Suzumura A, et al. Thermoelectric properties of binary semiconducting intermetallic compounds Al<sub>2</sub>Ru and Ga<sub>2</sub>Ru synthesized by spark plasma sintering process. *Mater Trans* 2010;51:988–93.
- [36] Takagiwa Y, Kitahara K, Matsubayashi Y, et al. Thermoelectric properties of FeGa<sub>3</sub>-type narrow-bandgap intermetallic compounds Ru(Ga, In)<sub>3</sub>: experimental and calculational studies. *J Appl Phys* 2012;111:123707.
- [37] Alvarez-Quiceno J, Dalpian G, Fazzio A, et al. Semiclassical transport properties of IrGa<sub>3</sub>: a promising thermoelectric material. *J Phys Condens Matter* 2018;30:085701.
- [38] Taranova A, Novitskii A, Voronin A, et al. Influence of V doping on the thermoelectric properties of Fe<sub>2</sub>Ti<sub>1-x</sub>V<sub>x</sub>Sn heusler alloys. *Semiconductors* 2019;53:768–71.
- [39] Rai D, Sandeep Shankar A, et al. Electronic, optical, and thermoelectric properties of Fe<sub>2+x</sub>V<sub>1-x</sub>Al. *AIP Adv* 2017;7:045118.
- [40] Wagner M, Cardoso-Gil R, Oeschler N, et al. RuIn<sub>3-x</sub>Sn<sub>x</sub>, RuIn<sub>3-x</sub>Zn<sub>x</sub>, and Ru<sub>1-y</sub>In<sub>3</sub>-new thermoelectrics based on the semiconductor RuIn<sub>3</sub>. *J Mater Res* 2011;26:1886.
- [41] Buffon ML, Laurita G, Lamontagne L, et al. Thermoelectric performance and the role of anti-site disorder in the 24-electron Heusler TiFe<sub>2</sub>Sn. *J Phys Condens Matter* 2017;29:405702.
- [42] Lue CS, Ross Jr JH, Rathnayaka K, et al. Superparamagnetism and magnetic defects in Fe<sub>2</sub>VAl and Fe<sub>2</sub>VGa. *J Phys Condens Matter* 2001;13:1585.
- [43] Endo K, Matsuda H, Ooiwa K, et al. Anomalous GMR in Fe<sub>2-x</sub>V<sub>1-x</sub>Ga and Fe<sub>2-y</sub>V<sub>1-y</sub>Al. *J Magn Magn Mater* 1998;177:1437–8.
- [44] Chen C, Wu W, Yu Z, et al. Graphyne as a second-order and real Chern topological insulator in two dimensions. *Phys Rev B* 2021;104:085205.
- [45] Lee E, Kim R, Ahn J, et al. Two-dimensional higher-order topology in monolayer graphdiyne. *NPJ Quantum Mater* 2020;5:1–7.
- [46] Liu F, Wakabayashi K. Higher-order topology and fractional charge in monolayer graphene. *Phys Rev Res* 2021;3:023121.
- [47] Benalcazar WA, Li T, Hughes TL. Quantization of fractional corner charge in C<sub>n</sub> symmetric higher-order topological crystalline insulators. *Phys Rev B* 2019;99:245151.
- [48] Zhang S, Xie M, Li F, et al. Semiconducting group 15 monolayers: a broad range of band gaps and high carrier mobilities. *Angew Chem* 2016;128:1698–1701.
- [49] Ares P, Aguilar-Galindo F, Rodríguez-San-Miguel D, et al. Mechanical isolation of highly stable antimonene under ambient conditions. *Adv Mater* 2016;28:6332–6.
- [50] Ji J, Song X, Liu J, et al. Two-dimensional antimonene single crystals grown by van der Waals epitaxy. *Nat Commun* 2016;7:1–9.
- [51] Schindler F, Brzeziska M, Benalcazar WA, et al. Fractional corner charges in spin-orbit coupled crystals. *Phys Rev Res* 2019;1:033074.
- [52] Radha SK, Lambrecht WRL. Buckled honeycomb antimony: higher order topological insulator and its relation to the Kekulé lattice. *Phys Rev B* 2020;102:115104.
- [53] Nie S, Bernevig BA, Wang Z. Sixfold excitations in electrides. *Phys Rev Res* 2021;3:L012028.
- [54] Araujo RE, Corbett JD. Lanthanum monochloride and lanthanum sesquichloride. *Inorg Chem* 1981;20:3082–6.
- [55] Xie LS, Schoop LM, Seibel EM, et al. A new form of Ca<sub>3</sub>P<sub>2</sub> with a ring of Dirac nodes. *APL Mater* 2015;3:083602.
- [56] Kang JK, Lee JY, Muller RP, et al. Hydrogen storage in LiAlH<sub>4</sub>: predictions of the crystal structures and reaction mechanisms of intermediate phases from quantum mechanics. *J Chem Phys* 2004;121:10623–33.
- [57] Choi YJ, Lu J, Sohn HY, et al. Reaction mechanisms in the Li<sub>3</sub>AlH<sub>6</sub>/LiBH<sub>4</sub> and Al/LiBH<sub>4</sub> systems for reversible hydrogen storage. Part 1: H capacity and role of Al. *J Phys Chem C* 2011;115:6040–7.
- [58] Sujan G, Pan Z, Li H, et al. An overview on TiFe intermetallic for solid-state hydrogen storage: microstructure, hydrogenation and fabrication processes. *Crit Rev Solid State Mater Sci* 2020;45:410–27.
- [59] Halicioğlu R, Bayrak M, İscan B, et al. An experimental study on hydrogen storage capabilities improvement of the TiFeH<sub>2</sub>. *Energy Sources A* 2012;34:1876–82.
- [60] Burchardt T. Hydrogen evolution on NiP<sub>x</sub> alloys: the influence of sorbed hydrogen. *Int J Hydrog Energy* 2001;26:193–8.
- [61] Wang TW, Wang TL, Chou WJ, et al. First-principles investigation of the hydrogen evolution reaction of transition metal phosphides CrP, MnP, FeP, CoP, and NiP. *Phys Chem Chem Phys* 2021;23:2305–12.
- [62] Owens-Baird B, Xu J, Petrovykh DY, et al. NiP<sub>2</sub>: a story of two divergent polymorphic multifunctional materials. *Chem Mater* 2019;31:3407–18.
- [63] Gillot F, Boyanov S, Dupont L, et al. Electrochemical reactivity and design of NiP<sub>2</sub> negative electrodes for secondary Li-ion batteries. *Chem Mater* 2005;17:6327–37.
- [64] Hayashi A, Inoue A, Tatsumisago M. Electrochemical performance of NiP<sub>2</sub> negative electrodes in all-solid-state lithium secondary batteries. *J Power Sources* 2009;189:669–71.
- [65] Alcantara R, Tirado J, Jumas J, et al. Electrochemical reaction of lithium with CoP<sub>3</sub>. *J Power Sources* 2002;109:308–12.
- [66] Jiang J, Li Z, He X, et al. Novel skutterudite CoP<sub>3</sub> based asymmetric supercapacitor with super high energy density. *Small* 2020;16:2000180.
- [67] Fullenwarth J, Darwiche A, Soares A, et al. NiP<sub>3</sub>: a promising negative electrode for Li- and Na-ion batteries. *J Mater Chem A* 2014;2:2050–9.
- [68] Lv B, Zhu XY, Lorenz B, et al. Superconductivity in the Mn<sub>5</sub>Si<sub>3</sub>-type Zr<sub>5</sub>Sb<sub>3</sub> system. *Phys Rev B* 2013;88:134520.
- [69] McMillan WL. Transition temperature of strong-coupled superconductors. *Phys Rev* 1968;167:331–44.
- [70] Allen PB, Dynes RC. Transition-temperature of strong-coupled superconductors reanalyzed. *Phys Rev B* 1975;12:905–22.
- [71] Gao J, Peng S, Wang Z, et al. Electronic structures and topological properties in nickelates Ln<sub>n+1</sub>Ni<sub>n</sub>O<sub>2n+2</sub>. *Natl Sci Rev* 2020;8:nwaa218.
- [72] Malyi OI, Varignon J, Zunger A. Bulk NdNiO<sub>2</sub> is thermodynamically unstable with respect to decomposition while hydrogenation reduces the instability and transforms it from metal to insulator. arXiv:2107.01790, 2021.
- [73] Xu Y, Elcoro L, Song ZD, et al. Filling-enforced obstructed atomic insulators. arXiv:2106.10276, 2021.
- [74] Xu Y, Elcoro L, Li G, et al. Three-dimensional real space invariants, obstructed atomic insulators and a new principle for active catalytic sites. arXiv:2111.02433, 2021.
- [75] Li G, Xu Y, Song Z, et al. Obstructed surface states as the origin of catalytic activity in inorganic heterogeneous catalysts. arXiv:2111.02435, 2021.



Jiacheng Gao is a graduate student of the Institute of Physics, Chinese Academy of Sciences. He is working on the field of topological band theory, topological materials and first-principles calculations. He is interested in the dynamical mean field theory and machine learning.



Miao Liu is an associate professor of Materials Science at the Institute of Physics, Chinese Academy of Sciences. His interest revolves around data-driven materials science.



Yuting Qian received her Ph.D. degree from the Institute of Physics, Chinese Academy of Sciences in 2021. Now she is a postdoc of the Correlated Quantum Matter Theory Team at the Center for Correlated Electron Systems (CCES), Seoul National University. She is working on the topological states by first-principle calculations.



Hongming Weng obtained his B.S. degree (2000) and Ph. D. degree (2005) from Nanjing University. He then worked at Tohoku University and Japan Advanced Institute of Science and Technology before joining the Institute of Physics, Chinese Academy of Sciences in 2010. His current research interest focuses on first-principle calculations on topological quantum states, magneto-optic Kerr effect and non-linear optical effects.



Huaxian Jia obtained his B.S. degree from Jilin University in 2017. He is currently a Ph.D. candidate at the Institute of Physics, Chinese Academy of Sciences. His research interest mainly focuses on the design of novel materials based on structure-properties relationships combined with data-driven approaches.



Zhijun Wang got his Ph.D. degree from the Institute of Physics (IOP), Chinese Academy of Sciences in 2014. Then he moved to Princeton University as a post-doc for 4 years, and joined IOP in 2018. He works on materials computation based on density functional theory. His current research interest focuses on novel topological and functional materials, correlation physics, and topological superconductors.